Surface Plasmon Resonance Sensor Based on Double-Sided Polished Microstructured Optical Fiber Coated With Graphene-on-Silver Layers

Donglian Hou [ID], Nannan Luan [ID], Xianxing Ji [ID], Wandi Zhang, Zhiwei Zhang, Xia Jiang, Li Song, Yaoyao Qi [ID], and Jianfei Liu

Abstract—We propose a concept of surface plasmon resonance sensor based on double-sided polished microstructured optical fiber coated with graphene-on-silver layers. The silver films on the polishing planes are covered with multilayer graphene which can prevent the oxidation of silver and enhance the adsorption of biomolecules. The sensing performance of the proposed sensors with polishing planes angle of 0°, 60° and 120°, are investigated by using both wavelength and amplitude interrogations. Our numerical results demonstrate that increasing the size of the air hole in the core area can effectively improve the wavelength and maximum amplitude sensitivities. Moreover, growing number layer of graphene can increase wavelength sensitivity, whereas decrease the maximum amplitude sensitivity.

Index Terms—Microstructured optical fiber, optical fiber sensors, refractive index, surface plasmon resonance.

I. INTRODUCTION

SURFACE plasmon resonance (SPR) sensors have been extensively studied over the recent decades due to their unique functions, playing an important role in industrial applications, such as bio-sensing, medical diagnostics, food safety, chemical analysis, gas detection and so on [1]–[16]. A conventional SPR sensor is based on Kretschmann setup, widely adopting the prism and metal with opposite dielectric constants to excite the electron density oscillations [17], [18]. Despite the sensing performance of SPR sensors based on prism is now relatively stable, these SPR sensors have some disadvantages of bulky volume and limited operation, which makes it unsuitable for miniaturization and remote sensing. As a new alternative solution, the optical fiber has emerged to replace it because of absolute advantages of miniaturization, high integration and remote sensing [1]–[16]. Many optical fiber based SPR sensors with different structures have been proposed for higher sensitivity and resolution [1]–[7].

Multi-mode fiber (MMF) and single-mode fiber (SMF) are used in SPR sensor earlier because they are the most common optical fibers and are easy to preparation [5]–[7]. However, the probe needs to be polished and tapered in the SMF-SPR sensors, which makes it very breakable and detection more restrictive. Besides, there are many modes and propagations of MMF-SPR sensors, which leads to spectrum broadening, thus the degradation of sensing performance [5]–[7].

In recent years, microstructured optical fiber (MOF) has been paid more attention by researchers, because they can provide better tunable optical properties through designing the microstructure, such as arrangement of cladding air holes and geometric configuration [1]–[7]. So far, numerous SPR sensors based on MOF have been presented [22]–[25], which possess high sensing performance, especially the ability of alleviating phase matching between the core mode and surface plasmon polariton (SPP) mode [22]–[25]. However, these MOF-SPR sensors need a deposition of plasmonic materials on the interior air holes of fiber, and causing their fabrications more difficult [22]–[25].

Moreover, there has strongly influence of metal coating on sensitivities of SPR sensors, considering that metal coating can transport many free electrons that supply negative dielectric constant [5], [6]. In previous studies, it has been proved that the sensing effect of MOF-SPR sensors with silver coating is better than that with gold coating, such as preferable sensitivity and narrower resonance peak [24]–[26]. With the limitations of oxidation and corrosion, however, silver compounds form on the surface in certain environments, which can lead to a descent in sensitivity. To ensure better sensitivity, it is necessary to take some reasonable protective measures that prevent silver from forming compounds.

To avoid the operating in the air holes and thus reducing the complexity of sensor fabrication, the D-shaped or side-opening MOFs have been used to fabricate the SPR sensors [26]–[40]. The open part of these MOFs can be made from the traditional MOFs by using mechanically polishing, chemically etching, femtosecond laser micromachining or focused ion beam technologies [41]–[43], and therefore the metal film and the analyte can be directly in contact with it. Taking advantage of these structures, in this paper, we propose a SPR sensor based on double-sided polished MOF coated with graphene-on-silver

layers for detecting the change of refractive index (RI). The main advantage of employing the double-sided polished structure is that it can provide the resonance peak with narrower spectral width, and thus contributing to a better signal to noise ratio (SNR) and sensing resolution [29]. One reason of using graphene is that it can prevent the oxidation and corrosion of silver [24]–[26], [28]. Previous studies have shown that graphene is an effective and reliable candidate, and its structure gives excellent electrical and optical properties [44], [45]. Graphene is a two-dimensional carbon material consisting of a layer of carbon atoms in a benzene ring structure that are periodically packed tightly together. This compact structure has a density of electrons that blocks the passage of atomic and molecules, acting as a protective layer on the top of silver [44], [45]. On the other hand, graphene is an ideal material for adsorbing molecules because of its large surface area and rich π configuration. It can act as a biomolecular recognition element (BRE) that can supply a prominent platform for adsorption of more biomolecules and consequently alter the propagation constant of SPP modes, creating a large RI variation on the graphene-silver interface [24]–[28], [44], [45]. By employing the graphene-silver coating as plasmonic materials, it is tremendous assistance in improving sensing performance of MOF-SPR sensors.

II. STRUCTURE AND THEORETICAL MODELING

The double-sided polished MOF-SPR sensor is based on common MOF with air holes arranged in a regular hexagon. In order to avoid the damage of air holes of cladding, we propose three feasible structures of the double-sided polishing, as shown in Fig. 1, which presents the structures with the angles between two polishing planes (θ) of 0°, 60° and 120° respectively. To carry out SPR for RI sensing, a thin layer of silver is located on the polished surface and then covered by the multilayer graphene, and forming the graphene-on-silver layer where the analyte can directly contact with it. Moreover, an air hole is designed in the center to lower the effective refractive index (n_{eff}) of the core mode, which attempts to promote the phase matching between the core mode and SPP mode [22]–[26]. The three structures in Fig. 1 have the same structural parameters, such as the diameter of the central air hole is $d_c = 0.1\Lambda$, the distance between the adjacent air holes is $\Lambda = 2$ μm, the polishing depth is $h = 1.2\Lambda$ and the thickness of silver layer is $m = 40$ nm.

In this work, the simulation is carried out by finite element method (FEM), adopting the perfectly matched layer (PML) as the boundary condition [24], [25]. The RI of silica is given by Sellimeiers equation [25], [27], [28]:

$$n^2(\lambda) = 1 + \frac{A_1\lambda^2}{\lambda^2 - B_1} + \frac{A_2\lambda^2}{\lambda^2 - B_2} + \frac{A_3\lambda^2}{\lambda^2 - B_3} \quad (1)$$

where λ is the wavelength in micrometer, Sellmeier coefficients A_1, A_2, A_3, B_1, B_2 and B_3 are referred to Ref. [25]. The dielectric constant of silver is defined by the Drude model [25]:

$$\varepsilon_{\text{Ag}}(\omega) = \varepsilon_\infty - \frac{\omega_p^2}{\omega(\omega + i\omega_\tau)} \quad (2)$$
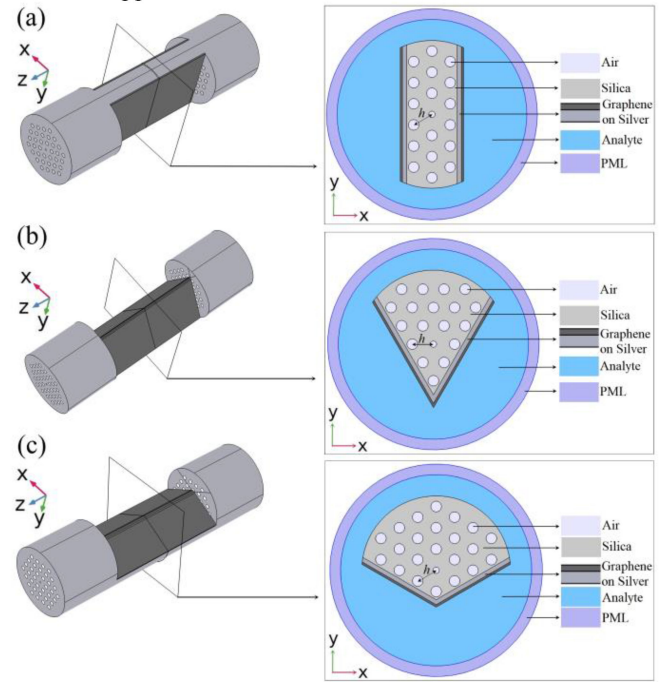

Fig. 1. The 3D and cross-sectional diagrams of SPR sensors based on double-sided polished MOF coated with graphene-on-silver layers whose angles between two polishing planes (θ) are (a) 0°, (b) 60° and (c) 120°, respectively.

where $\varepsilon_\infty = 9.84$, $\omega_p = 1.36 \times 10^{16}$, and $\omega_\tau = 1.018 \times 10^{14}$. The complex RI of graphene is described by the following equation [25]–[28]:

$$n_g = 3 + iC_1\lambda/3 \quad (3)$$

where λ is the vacuum wavelength and $C_1 \approx 5.446$ μm^{-1}. The RI of air is supposed to be 1.

III. RESULT

The modal analysis is carried out on the XY plane, while the light propagates in the fiber core along the z-axis direction, as shown in Fig. 1. In our calculation, it is assumed that the thickness of monolayer graphene is equal to 0.34 nm and the number of layers of graphene (N) is 3 [26]–[28]. Since SPP mode generated at the interface has the polarized direction being vertical to the graphene-silver layer [27]–[35], [38], [40], only x-polarized core mode is coupled with it when the structure with $\theta = 0°$, as shown in Fig. 1(a). Fig. 2 shows the loss curves of x-polarized core mode of double-sided polished MOF-SPR sensor with $\theta = 0°$ when the analyte RI (n_a) is 1.33 and 1.34, respectively. As seen from Fig. 2, the wavelength of resonance peak of x-polarized core mode is 490.1 nm at $n_a = 1.33$, where the maximum loss is 23.22 dB/cm. The insets in the Fig. 2 display mode field distributions of points A and B on the loss curve of $n_a = 1.33$, which can obviously show the energy transfer between the core mode and SPP mode. The inset B clearly presents the mode field profile of the core mode coupled with SPP mode at resonance wavelength of 490.1 nm. For comparison, the inset A presents the mode field profile of the core mode at the nonresonance wavelength of 400 nm.
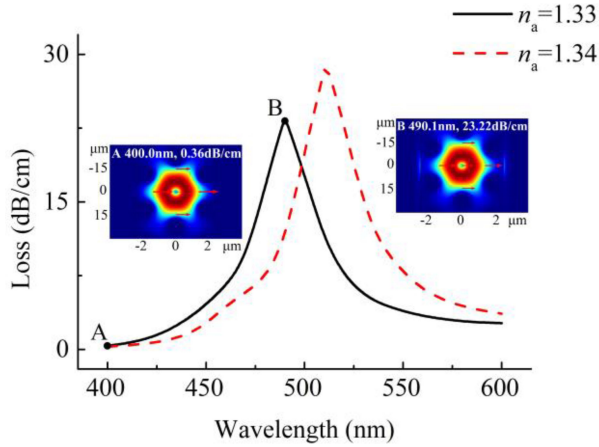
Fig. 2. Loss spectra of *x*-polarized core mode of the double-sided polished MOF-SPR sensor with $\theta = 0°$. Insets A and B show electric field distributions of core mode at the corresponding wavelengths A and B on the loss curve for $n_a = 1.33$.

In the other two structures with $\theta = 60°$ and $120°$ as shown in Fig 1(b) and (c), the SPP modes on graphene-on-silver layer have the polarization in both *x* and *y* directions, in consequence, that can couple with the *x*- and *y*-polarized core modes. Figs. 3 and 4 respectively show the loss spectra of the core modes of structures with $\theta = 60°$ and $120°$ for the change of n_a from 1.33 to 1.34 and the mode field distributions of the core modes at the nonresonance and resonance wavelengths with $n_a = 1.33$. As seen from the Figs. 3 and 4, due to the different structures, the energy distribution in the *x*- and *y*- polarized directions is different. Because the polarization direction of the electric field of the excited SPP mode is perpendicular to the metal coated plane, the change of polishing plane angle will cause the change of *x*- and *y*- polarized components of SPP mode, resulting in different coupling degree between these two components and core mode. The intensity of the *x*-polarized resonance peak is stronger than that of the *y*-polarized resonance peak for the structure with $\theta = 60°$ (see the inset B in the Fig. 3), whereas the intensity of the *y*-polarized resonance peak is stronger than that of the *x*-polarized resonance peak for the structure with $\theta = 120°$ (see the inset B in the Fig. 4).

The different resonance peaks excited by the three proposed sensor structures could lead to different sensing performance for the RI sensing. In next part, we study and compare the sensing performance of the three structures in the wavelength and amplitude interrogations respectively.

A. Wavelength Interrogation

As n_a becomes larger, the loss of resonance peak increases and the resonance peak moves to a longer wavelength, as shown in Figs. 2–4. The effect of change in n_a on the shift of resonance peak wavelength is an important index to evaluate the performance of sensor. In the wavelength interrogation, the change in n_a (Δn_a) can be detected by measuring the shift of resonance peak ($\Delta\lambda_{peak}$). The wavelength sensitivity (S_λ) is defined

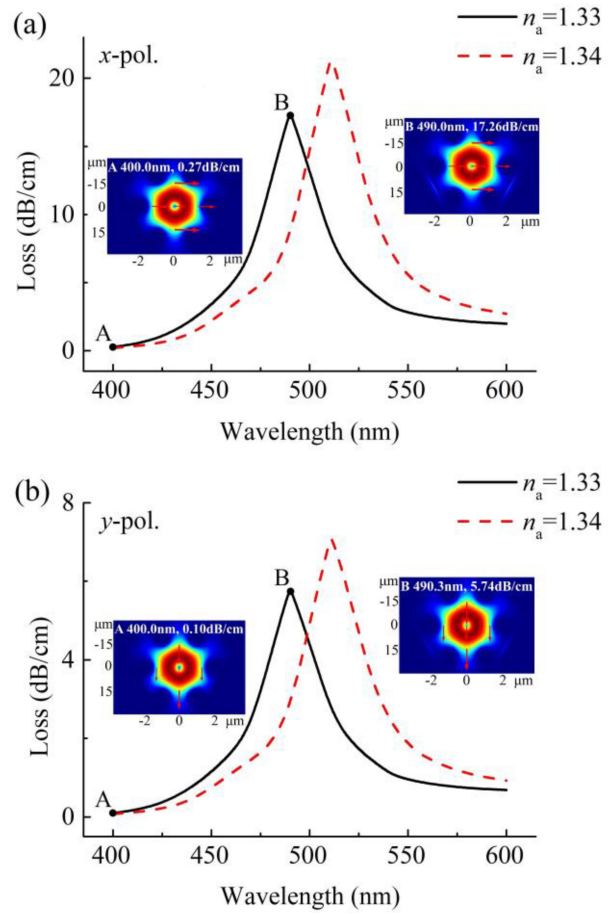Fig. 3. (a) Loss spectra of *x*-polarized and (b) *y*-polarized core modes of the proposed sensor with $\theta = 60°$ when n_a varies from 1.33 to 1.34. The insets show electric field distributions of *x*-polarized and *y*-polarized core modes at corresponding wavelengths for $n_a = 1.33$.

TABLE I
SUMMARY OF S_λ OF THE THREE SENSORS

| θ | Polarization | Peak Wavelength (nm) | | S_λ |
		n_a=1.33	n_a=1.34	(nm/RIU)
0°	*x*-pol.	490.1	510.8	2070
60°	*x*-pol.	490.2	510.9	2070
	y-pol.	490.3	511.0	2070
120°	*x*-pol.	490.2	510.9	2070
	y-pol.	489.9	510.5	2060

as [29]

$$S_\lambda \,(\text{nm/RIU}) = \frac{\Delta\lambda_{peak}}{\Delta n_a} \tag{4}$$

The peak wavelength and S_λ of the three structures have been summarized in Table I with the n_a range of 1.33–1.34. It can be seen that the three proposed structures have basically the same peak wavelength and S_λ.

B. Amplitude Interrogation

With the change of n_a, the loss of the resonance peak changes obviously. In the amplitude interrogation, therefore, the Δn_a
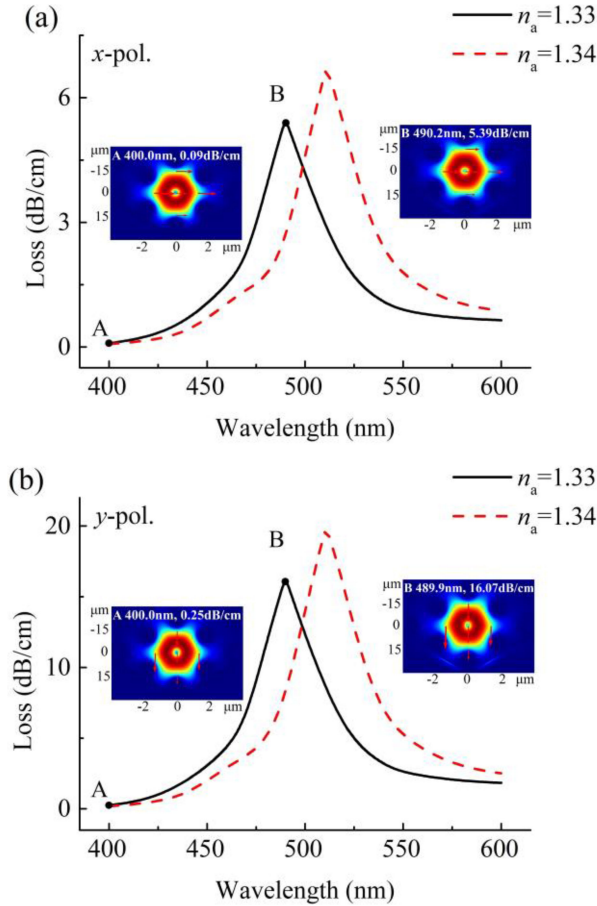
Fig. 5. Variation of S_A of the proposed sensor with $\theta = 0°$.

Fig. 4. (a) Loss spectra of x-polarized and (b) y-polarized core modes of the proposed sensor with $\theta = 120°$ when n_a varies from 1.33 to 1.34. The insets show electric field distributions of x-polarized and y-polarized core modes at corresponding wavelengths for $n_a = 1.33$.

Fig. 6. Loss spectra of x-polarized core mode of the sensor with $\theta = 0°$ for different d_c at $n_a = 1.33$. Insets A, B and C show electric field distributions of core modes at the corresponding wavelengths A, B and C on the loss curves.

TABLE II
SUMMARY OF MAX S_A FOR THE THREE SENSORS WITH DIFFERENT θ

θ	Polarization	Max S_A (RIU^{-1})	λ (nm)
0°	x-pol.	206.59	518.1
60°	x-pol.	206.11	518.2
	y-pol.	203.86	518.3
120°	x-pol.	204.16	518.2
	y-pol.	202.49	518.0

can be obtained by detecting the power of transmitted light at a certain wavelength (λ). The amplitude sensitivity (S_A) is defined as [29]

$$S_A(\text{RIU}^{-1}) = \frac{1}{\alpha(\lambda, n_a)} \cdot \frac{\Delta\alpha(\lambda, n_a)}{\Delta n_a} \quad (5)$$

where the $\alpha(\lambda, n_a)$ is the propagation loss of core mode at $n_a = 1.33$ and $L = 1/\alpha(\lambda, n_a)$ is the length of sensor. The S_A curve of the structure with $\theta = 0°$ is shown in Fig. 5, where the maximum S_A is 206.59 RIU^{-1} appearing at 518.1 nm.

From Table II, it can be seen that there is not much difference in the maximum S_A of the three proposed structures, appearing near the wavelength of 518 nm. However, their maximum S_A,
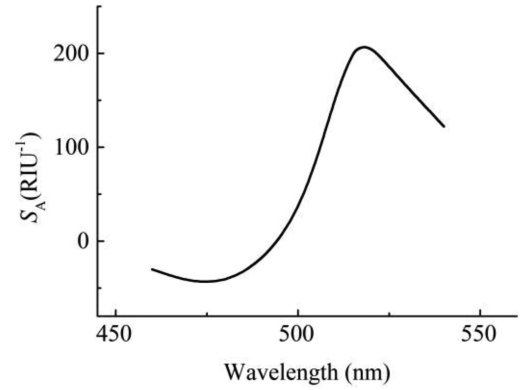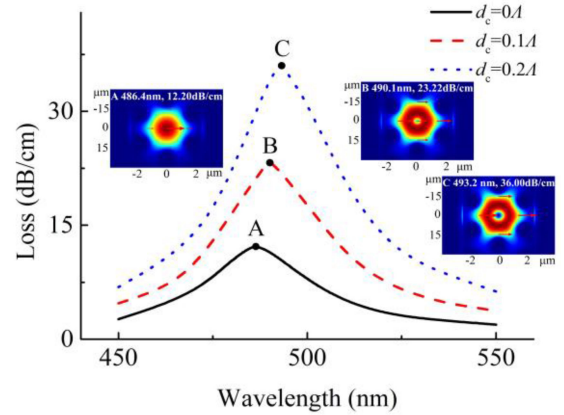
including x-polarized of structure with $\theta = 0°$, x-polarized of structure with $\theta = 60°$ and y-polarized of structure with $\theta = 120°$, can be achieved by requiring a shorter L, because their losses of core mode are larger than that of other polarized core mode, as shown in Figs. 2–4.

Table III shows the comparison of sensitivities for different MOF-SPR sensors. Compared with the inside gold coated structure, the proposed structure has greater wavelength sensitivity when n_a varies from 133 to 1.34 [22]. Among the four structures in Table III, the proposed structure has the largest amplitude sensitivity because it exhibits a narrower spectral width [22], [29], [30].

IV. DISCUSSION

A. Influence of the Diameter of Air Hole in the Core Area on Sensing Performance

The introduction of air hole reduces n_{eff} of the core region and hence reduces the confinement of the guided mode. That pushes more light towards the cladding region and hence increases the coupling to SPP causing loss and sensitivity to increase [22]–[26]. And thus the diameter of air hole in the core area (d_c) has a significant impact on the sensing performance [28]–[30], [34]. Figs. 6–8 present respectively the loss spectra of the sensors

TABLE III
COMPARISON OF SENSITIVITIES FOR DIFFERENT MOF-SPR SENSORS

Fiber structure	Wavelength(nm)	RI Range	Interrogation	Sensitivity	Ref.
Inside gold coated MOF	500-700	1.33-1.34	Wavelength	1000nm/RIU	[22]
D-shaped MOF	550-750	1.33-1.34	Wavelength	2900 nm/RIU	[30]
			Amplitude	129.21RIU^{-1}	
Double-sided polished MOF	500-700	1.33-1.34	Wavelength	1300nm/RIU	[29]
			Amplitude	120RIU^{-1}	
Double-sided polished MOF with graphene-on-silver layers	450-550	1.33-1.34	Wavelength	2060-2070 nm/RIU	This work
			Amplitude	202.49-206.59RIU^{-1}	
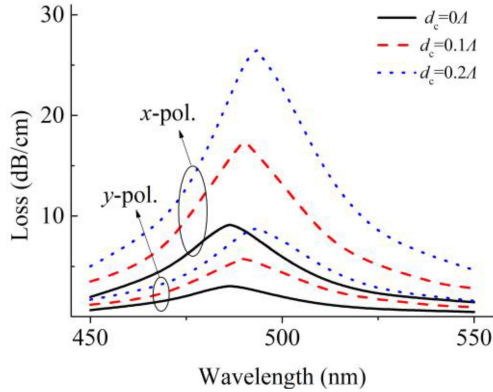
Fig. 7. Loss spectra of *x*-polarized and *y*-polarized core modes of the sensor with $\theta = 60°$ for different d_c at $n_a = 1.33$.
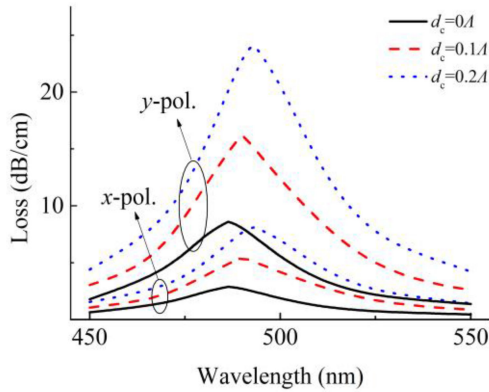
Fig. 8. Loss spectra of *x*-polarized and *y*-polarized core modes of the sensor with $\theta = 120°$ for different d_c at $n_a = 1.33$. .

TABLE IV
SUMMARY OF S_λ OF THE THREE SENSORS WITH DIFFERENT D_C

θ	Polarization	S_λ (nm/RIU)		
		$d_c=0\Lambda$	$d_c=0.1\Lambda$	$d_c=0.2\Lambda$
0°	*x*-pol.	1990	2070	2150
60°	*x*-pol.	1980	2070	2150
	y-pol.	1990	2070	2150
120°	*x*-pol.	1990	2070	2150
	y-pol.	1970	2060	2140

TABLE V
SUMMARY OF S_A OF THE THREE SENSORS WITH DIFFERENT D_C

θ	Polarization	$d_c=0\Lambda$		$d_c=0.1\Lambda$		$d_c=0.2\Lambda$	
		Max S_A (RIU^{-1})	λ (nm)	Max S_A (RIU^{-1})	λ (nm)	Max S_A (RIU^{-1})	λ (nm)
0°	*x*-pol.	202.03	513.4	206.59	518.1	210.55	522.0
60°	*x*-pol.	201.74	513.5	206.11	518.2	209.84	522.2
	y-pol.	199.67	513.5	203.86	518.3	207.28	522.2
120°	*x*-pol.	200.30	513.5	204.16	518.2	207.29	522.2
	y-pol.	198.74	513.4	202.49	518.0	205.60	522.1

TABLE VI
SUMMARY OF S_λ OF THE THREE SENSORS WITH DIFFERENT N

θ	Polarization	S_λ (nm/RIU)				
		N=1	N=2	N=3	N=4	N=5
0°	*x*-pol.	2030	2050	2070	2090	2110
60°	*x*-pol.	2040	2050	2070	2090	2100
	y-pol.	2040	2060	2070	2090	2110
120°	*x*-pol.	2040	2050	2070	2090	2110
	y-pol.	2030	2040	2060	2070	2100

with $\theta = 0°$, 60° and 120°, for different d_c at $n_a = 1.33$. As shown, the changes of the resonance peaks caused by the d_c changing in the three sensors show a similar tendency. Taking the proposed structure with $\theta = 0°$ as an example (see Fig. 6), as d_c increases from 0Λ to 0.2Λ, the peak loss gradually moves towards a longer wavelength and its corresponding amplitude increases obviously, which means stronger coupling between the core mode and SPP mode. The peak loss of 12.20 dB/cm is at 486.4 nm for $d_c = 0\Lambda$ while the peak loss of 36.00 dB/cm is at 493.2 nm for $d_c = 0.2\Lambda$. This indicates that the larger d_c is, the smaller n_{eff} of core area becomes, thus further facilitating phase matching and transferring more energy from the core mode to SPP mode, as the insets A-C shown in Fig. 6.

The S_λ and maximum S_A also are affected by the change of d_c. As shown in the Table IV, S_λ increases with the increase of d_c,

such as S_λ from 1990 nm/RIU with $d_c = 0\Lambda$ to 2150 nm/RIU with $d_c = 0.2\Lambda$ for the structure with $\theta = 0°$. Moreover, the maximum S_A also shows a slight increasing trend and occurs at the longer wavelength, as shown in Table V. For instance, the max S_A increases from 202.03 RIU^{-1} at 513.4 nm with $d_c = 0\Lambda$ to 210.55 RIU^{-1} at 522.0 nm with $d_c = 0.2\Lambda$ for the structure with $\theta = 0°$. In general, increasing the size of the air hole in the core area can improve effectively the sensing performance of the proposed sensors.

B. Influence of the Number Layers of Graphene on Sensing Performance

The difference in the thickness layer of graphene can affect the sensing performance of sensor, by varying the number layers (N) of graphene. Here, the maximum N is 5, because the electronic

TABLE VII
SUMMARY OF MAX S_A OF THE THREE SENSORS WITH DIFFERENT N

| θ	Polarization	N=1		N=2		N=3		N=4		N=5	
		Max S_A (RIU^{-1})	λ (nm)	Max S_A (RIU^{-1})	λ (nm)	Max S_A (RIU^{-1})	λ (nm)	Max S_A (RIU^{-1})	λ (nm)	Max S_A (RIU^{-1})	λ (nm)
0°	x-pol.	497.93	495.5	297.38	506.8	206.59	518.1	156.64	529.5	125.60	540.9
60°	x-pol.	496.03	495.6	296.52	506.9	206.11	518.2	156.29	529.6	125.33	540.9
	y-pol.	489.51	495.7	293.24	506.9	203.86	518.3	154.66	529.6	123.99	540.9
120°	x-pol.	491.31	495.6	293.83	506.9	204.16	518.2	154.79	529.6	124.09	541.0
	y-pol.	484.39	495.4	290.83	506.7	202.49	518.0	153.75	529.6	123.45	540.9
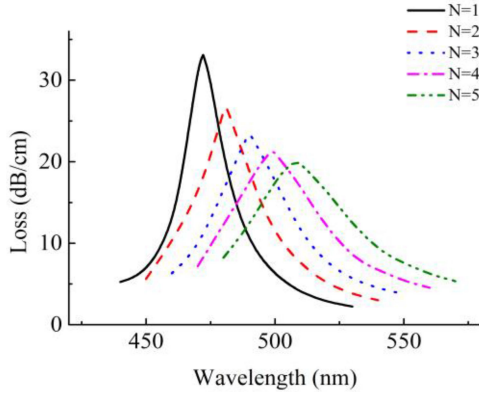
Fig. 9. Loss spectra of x-polarized core mode of the proposed sensor with $\theta = 0°$ for different N varying from 1 to 5 at $n_a = 1.33$.

Fig. 10. (a) Loss spectra of x-polarized and (b) y-polarized core modes of the proposed sensor with $\theta = 60°$ for different N varying from 1 to 5 at $n_a = 1.33$, respectively.

properties of graphene are gradually changed into that of bulk graphite if the N exceeds 5 [44]–[46]. With the increase of N, the corresponding peak loss decreases gradually and shifts to a longer wavelength for the sensor with $\theta = 0°$, as shown in Fig. 9. For the structure with N = 1, the maximum loss is 33.08 dB/cm at 472.1 nm, whereas for that of with N = 5, maximum loss is down to 19.86 dB/cm and shifts to 508.2 nm, when n_a is 1.33. The reason for this phenomenon is that the increase in the thickness of graphene leads to the growth of n_{eff} of the SPP mode at metal dielectric layer, which requires a longer wavelength to satisfy the coupling between the core mode and SPP mode [28]. Note that the spectral width of the resonance peak is broadened gradually with the increase of N. The imaginary part of the dielectric constant of graphene can cause damping loss that becomes bigger with the increase of graphene thickness. Most of the light, in the optical fiber, is used to overcome the damping loss, so the excitation of SPP mode becomes weaker, resulting in the reduction of the coupling between the two modes and loss in the core mode thus broadening the resonance spectrum [24]. Figs. 10 and 11 show loss spectra of x-polarized and y-polarized core modes of sensors with $\theta = 60°$ and 120°, respectively, whose trends are consistent with the results in Fig. 9. The peak losses of these two structures decrease and their resonance wavelengths shift to the right gradually due to the increase of N. The resonance spectra are also broadened because of the higher damping loss caused by the thicker layer of graphene.

To further comprehensively evaluate the effect of N on the sensing performance of the proposed sensors, we also explore the changes of S_λ and maximum S_A. According to variation of peak loss with n_a from 1.33 to 1.34, the S_λ can be calculated from (4). The effect of N on S_λ is shown in the Table VI. It is much easier observed that the S_λ of the three proposed structures basically have the slow growth with the increase in N. In addition, the S_A is also affected by N for the same structure. According to (5), the maximum S_A of the three proposed structures with different N from 1 to 5, are summarized more roundly in the Table VII. Taking the proposed structure with $\theta = 0°$ as an example, the maximum S_A decreases from 497.93 RIU^{-1} at 495.5 nm for N = 1 to 125.60 RIU^{-1} at 540.9 nm for N = 5. The growth of graphene thickness leads to reduced loss of the core mode, which results in a smaller maximum S_A. Therefore, optimizing the thickness of graphene is also an important aspect to improve the performance of the proposed sensors.
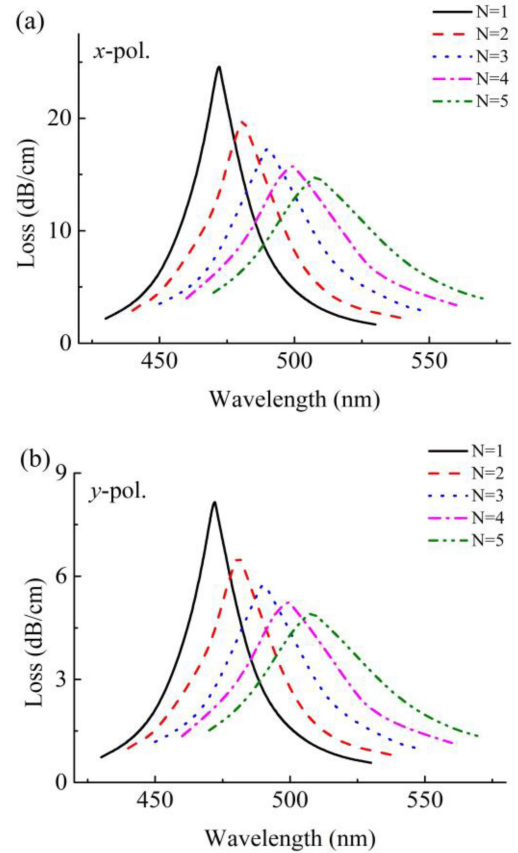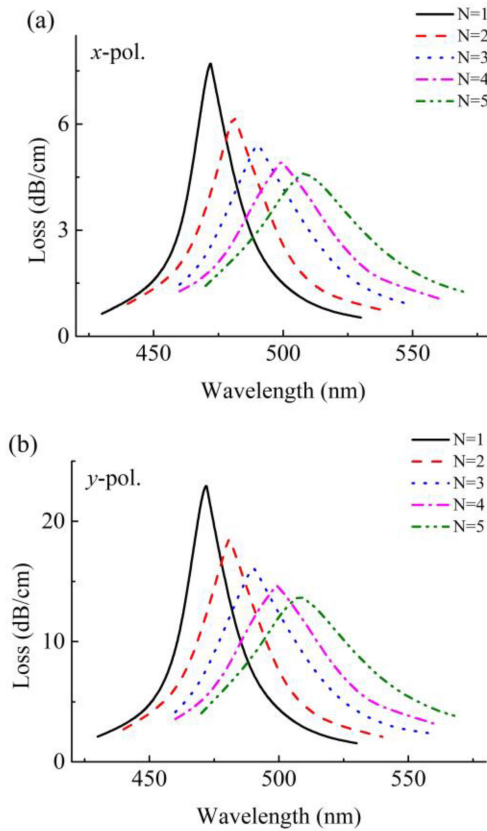
Fig. 11.   (a) Loss spectra of *x*-polarized and (b) *y*-polarized core modes of the proposed sensor with $\theta = 120°$ for different N varying from 1 to 5 at $n_a = 1.33$, respectively.

V. Conclusion

In conclusion, we design a novel SPR sensor based on double-sided polished MOF coated with graphene-on-silver layers. The multilayer graphene can prevent silver layer from oxidation and enhance the adsorption of biomolecules. We investigate the sensing performance of the proposed structures with $\theta = 0°$, $60°$ and $120°$, as well as the effects of the structural parameters including d_c and N. Our results demonstrate that the increase in d_c effectively improves S_λ and maximum S_A. Moreover, the growing N can increase S_λ, whereas decrease the maximum S_A. Owing to their excellent sensing performance and good stability, the proposed sensors with the multilayer graphene are expected to be a great contender in the biosensor field.

References

[1] M. Gandhi, S. Chu, K. Senthilnathan, P. Babu, K. Nakkeeran, and Q. Li, "Recent advances in plasmonic sensor-based fiber optic probes for biological applications," *Appl. Sci. (Basel)*, vol. 9, no. 5, Mar. 2019, Art. no. 949.

[2] Y. Xu *et al.*, "Optical refractive index sensors with plasmonic and photonic structures: Promising and inconvenient truth," *Adv. Opt. Mater.*, vol. 7, no. 9, May 2019, Art. no. 1801433.

[3] Q. Duan, Y. Liu, S. Chang, H. Chen, and J. H. Chen, "Surface plasmonic sensors: Sensing mechanism and recent applications," *Sensors (Basel)*, vol. 21, no. 16, Aug. 2021, Art. no. 5262.

[4] M. E. Martínez-Hernández, P. J. Rivero, J. Goicoechea, and F. J. Arregui, "Trends in the implementation of advanced plasmonic materials in optical fiber sensors (2010–2020)," *Chemosensors*, vol. 9, no. 4, Apr. 2021, Art. no. 64.

[5] A. K. Sharma, A. K. Pandey, and B. Kaur, "A review of advancements (2007–2017) in plasmonics-based optical fiber sensors," *Opt. Fiber Technol.*, vol. 43, pp. 20–34, Jul. 2018.

[6] E. Klantsataya, P. Jia, H. Ebendorff-Heidepriem, T. M. Monro, and A. Francois, "Plasmonic fiber optic refractometric sensors: From conventional architectures to recent design trends," *Sensors (Basel)*, vol. 17, no. 1, Jan. 2017, Art. no. 12.

[7] Y. Liu and W. Peng, "Fiber-optic surface plasmon resonance sensors and biochemical applications: A review," *J. Lightw. Technol.*, vol. 39, no. 12, pp. 3781–3791, Jun. 2021.

[8] F. Haider, R. Ahmmed Aoni, R. Ahmed, W. Jen Chew, and G. Amouzad Mahdiraji, "Plasmonic micro-channel based highly sensitive biosensor in visible to mid-IR," *Opt. Laser Technol.*, vol. 140, Aug. 2021, Art. no. 107020.

[9] H. Zhou, K. Ding, Q. Yu, H. Wang, J. Liu, and Z. Wang, "Enhanced electrochemiluminescence ratiometric cytosensing based on surface plasmon resonance of au nanoparticles and nanosucculent films," *Bionsens. Bioelectron.*, vol. 189, Jun. 2021, Art. no. 113367.

[10] W. Jing, A. Hunt, N. Tao, F. Zhang, and S. Wang, "Simultaneous quantification of protein binding kinetics in whole cells with surface plasmon resonance imaging and edge deformation tracking," *Membranes (Basel)*, vol. 10, no. 9, Sep. 2020, Art. no. 247.

[11] N. An *et al.*, "A multiplex and regenerable surface plasmon resonance (MR-SPR) biosensor for DNA detection of genetically modified organisms," *Talanta*, vol. 231, Aug. 2021, Art. no. 122361.

[12] Y.-F. Chang, Y.-T. Chou, C.-Y. Cheng, J.-F. Hsu, L.-C. Su, and J. A. Ho, "Amplification-free detection of cytomegalovirus miRNA using a modification-free surface plasmon resonance biosensor," *Anal. Chem.*, vol. 93, no. 22, pp. 8002–8009, Jun. 2021.

[13] S. Singh *et al.*, "2D nanomaterial-based surface plasmon resonance sensors for biosensing applications," *Micromachines (Basel)*, vol. 11, no. 8, Aug. 2020, Art. no. 779.

[14] M. M. Hossain and M. A. Talukder, "Gate-controlled graphene surface plasmon resonance glucose sensor," *Opt. Commun.*, vol. 493, Aug. 2021, Art. no. 126994.

[15] A. Ecija-Arenas, E. M. Kirchner, T. Hirsch, and J. M. Fernandez-Romero, "Development of an aptamer-based SPR-biosensor for the determination of kanamycin residues in foods," *Anal. Chim. Acta.*, vol. 1169, Aug. 2021, Art. no. 338631.

[16] Z. Liu, J. He, and S. He, "Characterization and sensing of inert gases with a high-resolution SPR sensor," *Sensors (Basel)*, vol. 20, no. 11, Jun. 2020, Art. no. 3295.

[17] R. Boruah, D. Mohanta, A. Choudhury, P. Nath, and G. A. Ahmed, "Surface plasmon resonance based protein biosensing using a kretschmann configured double prism arrangement," *IEEE Sens. J.*, vol. 15, no. 12, pp. 6791–6796, Dec. 2015.

[18] C. Lertvachirapaiboon, A. Baba, K. Shinbo, and K. Kato, "Dual-mode surface plasmon resonance sensor chip using a grating 3D-printed prism," *Anal. Chim. Acta.*, vol. 1147, pp. 23–29, Feb. 2021.

[19] A. K. Pathak and V. K. Singh, "SPR based optical fiber refractive index sensor using silver nanowire assisted CSMFC," *IEEE Photon. Technol. Lett.*, vol. 32, no. 8, pp. 465–468, Apr. 2020.

[20] W. Li, A. Zhang, Q. Cheng, C. Sun, and Y. Li, "Theoretical analysis on SPR based optical fiber refractive index sensor with resonance wavelength covering communication C+L band," *Optik*, vol. 213, Jul. 2020, Art. no. 164696.

[21] T. Wang *et al.*, "The effect of the TiO_2 film on the performance of the optical fiber SPR sensor," *Opt. Commun.*, vol. 448, pp. 93–97, Oct. 2019.

[22] A. Hassani and M. Skorobogatiy, "Design of the microstructured optical fiber-based surface plasmon resonance sensors with enhanced microfluidics," *Opt. Exp.*, vol. 14, no. 24, pp. 11616–11621, Nov. 2006.

[23] B. Shuai, L. Xia, and D. Liu, "Coexistence of positive and negative refractive index sensitivity in the liquid-core photonic crystal fiber based plasmonic sensor," *Opt. Exp.*, vol. 20, no. 23, pp. 25858–25866, Nov. 2012.

[24] A. A. Rifat, G. A. Mahdiraji, D. M. Chow, Y. G. Shee, R. Ahmed, and F. R. Adikan, "Photonic crystal fiber-based surface plasmon resonance sensor with selective analyte channels and graphene-silver deposited core," *Sensors (Basel)*, vol. 15, no. 5, pp. 11499–11510, May 2015.

[25] F. Wang, Z. Sun, C. Liu, T. Sun, and P. K. Chu, "A highly sensitive dual-core photonic crystal fiber based on a surface plasmon resonance biosensor with silver-graphene layer," *Plasmonics*, vol. 12, no. 6, pp. 1847–1853, Dec. 2016.

[26] J. N. Dash and R. Jha, "Graphene-based birefringent photonic crystal fiber sensor using surface plasmon resonance," *IEEE Photon. Technol. Lett.*, vol. 26, no. 11, pp. 1092–1095, Jun. 2014.

[27] G. An *et al.*, "Ultra-stable D-shaped optical fiber refractive index sensor with graphene-gold deposited platform," *Plasmonics*, vol. 14, no. 1, pp. 155–163, Jul. 2018.

[28] J. N. Dash and R. Jha, "On the performance of graphene-based D-shaped photonic crystal fibre biosensor using surface plasmon resonance," *Plasmonics*, vol. 10, no. 5, pp. 1123–1131, Oct. 2015.

[29] D. Hou *et al.*, "Surface plasmon resonance sensor based on double-sided polished microstructured optical fiber with hollow core," *IEEE Photon. J.*, vol. 13, no. 4, Aug. 2021, Art. no. 6800408.

[30] N. Luan, R. Wang, W. Lv, and J. Yao, "Surface plasmon resonance sensor based on D-shaped microstructured optical fiber with hollow core," *Opt. Exp.*, vol. 23, no. 7, pp. 8576–8582, Apr. 2015.

[31] H. Han *et al.*, "Surface plasmon resonance sensor based on dual-side polished microstructured optical fiber with dual-core," *Sensors*, vol. 20, no. 14, Jul. 2020, Art. no. 3911.

[32] N. Luan, L. Zhao, Y. Lian, and S. Lou, "A high refractive index plasmonic sensor based on D-shaped photonic crystal fiber with laterally accessible hollow-core," *IEEE Photon. J.*, vol. 10, no. 5, Sep. 2018, Art. no. 6803707.

[33] L. Zhao, H. Han, Y. Lian, N. Luan, and J. Liu, "Theoretical analysis of all-solid D-type photonic crystal fiber based plasmonic sensor for refractive index and temperature sensing," *Opt. Fiber Technol.*, vol. 50, pp. 165–171, Jul. 2019.

[34] N. Luan, H. Han, L. Zhao, J. Liu, and J. Yao, "Opening up dual-core microstructured optical fiber-based plasmonic sensor with large detection range and linear sensitivity," *Opt. Mater. Exp.*, vol. 9, no. 2, pp. 819–825, Feb. 2019.

[35] H. Han *et al.*, "A large detection-range plasmonic sensor based on an H-shaped photonic crystal fiber," *Sensors*, vol. 20, no. 4, Feb. 2020, Art. no. 3911.

[36] X. Yang, Z. Wang, Y. Liu, and J. Yao, "SPR sensor based on exposed core micro-structured optical fiber for salinity detection with temperature self-compensation," *Opt. Mater. Exp.*, vol. 11, no. 8, pp. 2468–2477, Aug. 2021.

[37] N. Luan and J. Yao, "Surface plasmon resonance sensor based on exposed-core microstructured optical fiber placed with a silver wire," *IEEE Photon. J.*, vol. 8, no. 1, Feb. 2016, Art. no. 4800508.

[38] N. Luan, C. Ding, and J. Yao, "A refractive index and temperature sensor based on surface plasmon resonance in an exposed-core microstructured optical fiber," *IEEE Photon. J,* vol. 8, no. 2, Apr. 2016, Art. no. 4801608.

[39] M. A. Mollah and M. S. Islam, "Novel single hole exposed-suspended core localized surface plasmon resonance sensor," *IEEE Sens. J.*, vol. 21, no. 3, pp. 2813–2820, Feb. 2020.

[40] N. Luan, R. Wang, W. Lv, and J. Yao, "Surface plasmon resonance sensor based on exposed-core microstructured optical fibres," *Electron. Lett.*, vol. 51, no. 9, pp. 714–715, Apr. 2015.

[41] C. J. Hensley, D. H. Broaddus, C. B. Schaffer, and A. L. Gaeta, "Photonic band-gap fiber gas cell fabricated using femtosecond micromachining," *Opt. Exp.*, vol. 15, no. 11, pp. 6690–6695, May 2007.

[42] A. van Brakel, C. Grivas, M. N. Petrovich, and D. J. Richardson, "Micro-channels machined in microstructured optical fibers by femtosecond laser," *Opt. Exp.*, vol. 15, no. 14, pp. 8731–8736, Jul. 2007.

[43] C. M. B. Cordeiro *et al.*, "Towards practical liquid and gas sensing with photonic crystal fibres: Side access to the fibre microstructure and single-mode liquid-core fibre," *Meas. Sci. Technol.*, vol. 18, no. 10, pp. 3075–3081, Oct. 2007.

[44] M. Saifur Rahman, M. S. Anower, L. B. Bashar, and K. A. Rikta, "Sensitivity analysis of graphene coated surface plasmon resonance biosensors for biosensing applications," *Sens. Biosens. Res.*, vol. 16, pp. 41–45, Nov. 2017.

[45] L. Wu, H. S. Chu, W. S. Koh, and E. P. Li, "Highly sensitive graphene biosensors based on surface plasmon resonance," *Opt. Exp.*, vol. 18, no. 14, pp. 14395–14400, Jul. 2010.

[46] K. F. Mak, M. Y. Sfeir, J. A. Misewich, and T. F. Heinz, "The evolution of electronic structure in few-layer graphene revealed by optical spectroscopy," *P. Nat. Acad. Sci. USA*, vol. 107, no. 34, pp. 14999–15004, Aug. 2010.